processes

Article

Numerical Investigation of Flow Characteristics for Gas–Liquid Two–Phase Flow in Coiled Tubing

Shihui Sun [1,*], Jiahao Liu [1], Wan Zhang [1] and Tinglong Yi [1]

Key Laboratory of Enhanced Oil Recovery, Ministry of Education, College of Petroleum Engineering, Northeast Petroleum University, Daqing 163318, China
* Correspondence: sshsmile@nepu.edu.cn

Abstract: Coiled tubing (CT) is widely used for horizontal well fracturing, squeeze cementing, and sand and solid washing in the oil and gas industry. During CT operation, a gas–liquid two-phase flow state appears in the tubing. Due to the secondary flow, this state produces a more extensive flow-friction pressure loss, which limits its application. It is crucial to understand the gas–liquid flow behavior in a spiral tube for frictional pressure drop predictions in the CT technique. In this study, we numerically investigated the velocity distribution and phase distribution of a gas–liquid flow in CT. A comparison of experimental data and simulated results show that the maximum average error is 2.14%, verifying the accuracy of the numerical model. The gas and liquid velocities decrease first and then rise along the axial direction due to the effect of gravity. Due to the difference in the gas and liquid viscosity, i.e., the flow resistance of the gas and liquid is different, the gas–liquid slip velocity ratio is always greater than 1. The liquid velocity exhibits a D-shaped step distribution at different cross-sections of spiral tubing. The secondary-flow intensity, caused by radial velocity, increases along the tubing. Due to the secondary-flow effect, the zone of the maximum cross-section velocity is off-center and closer to the outside of the tube. However, under the combined action of centrifugal force and the density difference between gas and liquid, the variation in the gas void fraction along the tubing is relatively stable. These research results are helpful in understanding the complex flow behavior of gas–liquid two-phase flow in CT.

Keywords: coiled tubing; gas–liquid two-phase flow; velocity distribution; phase distribution; friction pressure drop

Citation: Sun, S.; Liu, J.; Zhang, W.; Yi, T. Numerical Investigation of Flow Characteristics for Gas–Liquid Two–Phase Flow in Coiled Tubing. *Processes* **2022**, *10*, 2476. https://doi.org/10.3390/pr10122476

Academic Editors: Pietro Poesio and Andrea Aquino

Received: 25 October 2022
Accepted: 19 November 2022
Published: 22 November 2022

1. Introduction

Coiled tubing (CT) is widely applied in the oil and gas industry in horizontal well fracturing, squeeze cementing, and sand and solid washing due to its characteristics of high-pressure operation, fast running speed, robust construction timeliness, and high safety. During CT operation, a gas–liquid two-phase flow state appears in the tubing. When gas–liquid fluid flows through CT, a secondary flow perpendicular to the main flow direction is generated as a result of centrifugal force. The secondary vortex causes additional flow resistance in the coiled tubing, resulting in insufficient downhole hydraulic energy for the CT technique. Therefore, a clear understanding of the gas–liquid flow behavior in the spiral tube is essential to accurately predict flow friction to ensure the success of a CT operation.

In 1910, a water flow in a bent glass tube was observed using colored filaments by Eustice [1,2]. Dean studied the fluid flow in the helical section and proposed to use the Dean number to describe the effect of the centrifugal force on fluid flow in a spiral tube [3]. Based on experiment data, Berger established the empirical formula for the flow-friction coefficient of different fluids in curved and straight pipes [4,5]. Zhou used the boundary-layer theory to study the flow in a coiled tube [6]. Mccann deduced a flow model for the non-Newtonian fluid in CT and validated the model with full-size-flow experimental data [7]. Boersma used the large-eddy simulation (LES) to compute a fully developed turbulent flow in a curved pipe [8]. Zhang studied the influencing factors of the friction pressure drop in foam in CT using the numerical simulation method and analyzed the causes and characteristics of secondary flow [9]. Asafa studied the annulus fluid of coiled tubing in a horizontal well with the finite element method and established a prediction model for annular pressure drop [10]. Guan conducted experiments with different fluids and tubes with different curvature radii to investigate the flowing law in CT [11]. Wang used the CFD numerical simulation method to research the foam flow behavior in helical pipes [12]. Pereira conducted a full-scale experiment on Newtonian fluid flows in a spiral pipe [13]. Oliveira developed a mathematical model to simulate the pressure drop of Newtonian and non-Newtonian fluids along a coiled tube [14].

Studies of two-phase flow behavior in a helical tube have mainly concentrated on heat transfer and the chemical industry. Martinelli established an M–N estimation method for the pressure drop of a gas–water mixture under different pressures [15]. Lockhart proposed the L–M estimation method to predict the frictional pressure drop of a helical tube [16]. Akagawa concluded that the geometric parameters of spiral tubes would affect the frictional pressure drop [17]. Bi experimentally studied the frictional resistance of a high-pressure gas–water two-phase flow in vertical and horizontal spiral tubes [18]. Xin conducted a flow experiment in a curved pipe with water and air to measure the pressure drop and gas holdup [19]. Santini pointed out that centrifugal force significantly affects the fluid flow and heat transfer in a helical tube [20]. The frictional pressure drop of spiral tubes at different angles was measured by Guo [21]. Colombo numerically analyzed the gas–liquid two-phase flow in a spiral heat-exchange tube under adiabatic conditions [22]. Cioncolini summarized and analyzed 25 widely used empirical correlations and related data points in the published literature and proposed a frictional pressure drop prediction equation based on a homogeneous flow model [23]. Through experiments, Li and Zhao studied the frictional pressure drop of spiral pipes in a steam generator [24,25]. Wu established numerical models to investigate the two-phase-flow boiling heat transfer in a helically coiled tube [26,27].

Most research on the fluid in CT is limited to single-phase-fluid flow. There are limited studies of gas–liquid two-phase flows in spiral tubes focusing on heat transfer and the chemical industry, which is different from a CT's operating environment in the oil and gas industry. In addition, the diameters and lengths of CT vary greatly. Due to the limitations of experimental conditions and the complexity of the gas–liquid two-phase flow, there is no unified understanding of fluid flows in spiral tubes. In this study, considering the working conditions of CT operation, a gas–liquid two-phase flow in helical tubing was numerically simulated. The velocity distribution and phase distribution of gas and liquid were investigated. The research results are helpful in understanding the complex flow behavior of a gas–liquid two-phase flow in spiral pipes, and they lay a theoretical foundation for the establishment of a frictional pressure drop model for a CT system.

2. CFD Modeling for Gas–Liquid Two-Phase Flow

2.1. Governing Equations

Gas–liquid two-phase fluid is in an unbalanced state in the exchange of mass, momentum, and energy because of the gas–liquid interface. The flow parameters are difficult to unify. The Eulerian–Eulerian two-phase model regards gas and liquid as continuous flows moving through each other [28]. In any space, the sum of the volume rates of each phase is 1, and each phase follows its conservation law. Therefore, the model can accurately solve the phase parameters of a gas–liquid two-phase flow in spiral pipes and has been widely recognized in engineering. This study used the Eulerian–Eulerian two-phase fluid model to analyze gas and liquid behaviors in a helical tube.

The continuity equation for the gas and liquid phases is expressed in Equation (1).

$$\frac{\partial(\alpha_i \rho_i)}{\partial t} + \nabla \bullet (\alpha_i \rho_i \boldsymbol{v}_i) = 0 \tag{1}$$

Here, t is time; α, $\boldsymbol{v}$, and ρ are the volume fraction, velocity vector, and density, respectively. The variables with subscript $i = l$ are for liquid, and those with subscript $i = g$ are for gas.

The momentum conservation equation for the liquid and gas phases is written in Equation (2):

$$\frac{\partial(\alpha_i\rho_i\boldsymbol{v}_i)}{\partial t} + \nabla \bullet \left[\alpha_i\rho_i\boldsymbol{v}_i\boldsymbol{v}_i - \mu_i\left(\nabla\boldsymbol{v}_i + (\nabla\boldsymbol{v}_i)^T\right)\right] = \alpha_i(\rho_i g - \nabla P_i) + \boldsymbol{F}_{gl} \tag{2}$$

where μ is the effective dynamic viscosity coefficient, g is gravitational acceleration, $\boldsymbol{F}_{gl}$ is the virtual mass force between the gas and liquid phases, and P is pressure.

The gas void fraction is defined as:

$$\alpha_g = \frac{M_g}{M_g + M_l} \tag{3}$$

The relationship between the volume fraction of the liquid phase and gas phase is as follows:

$$\alpha_l + \alpha_g = 1 \tag{4}$$

The standard turbulence k-ε model is used to calculate the turbulent viscosity of the operation fluid [29]. The turbulent kinetic energy, k, and the specific dissipation rate, ε, can be calculated by Equations (5) and (6).

$$\frac{\partial(\rho_i k)}{\partial t} + \frac{\partial}{\partial x_i}(\rho_i k\boldsymbol{v}_i) = \frac{\partial}{\partial x_j}\left[\left(\mu_i + \frac{\mu_t}{\sigma_k}\right)\frac{\partial k}{\partial x_j}\right] + G_k + G_b - \rho_i\varepsilon - Y_M + S_k \tag{5}$$

$$\frac{\partial}{\partial t}(\rho_i\varepsilon) + \frac{\partial}{\partial x_i}(\rho_i\varepsilon u_i) = \frac{\partial}{\partial x_j}\left[\left(\mu_i + \frac{\mu_t}{\sigma_k}\right)\frac{\partial\varepsilon}{\partial x_j}\right] + C_{1\varepsilon}\frac{\varepsilon}{k}(G_k + C_{3\varepsilon}G_b) - C_{2\varepsilon}\rho_i\frac{\varepsilon^2}{k} + S_\varepsilon \tag{6}$$

The coefficient of turbulent viscosity, μ_t, is computed from:

$$\mu_t = \rho_i C_\mu \frac{k^2}{\varepsilon} \tag{7}$$

where G_k is the turbulent kinetic-energy generation because of the mean velocity gradients, G_b is the turbulent kinetic energy generated by buoyancy, and Y_M is the dissipation rate due to velocity turbulence. $C_{1\varepsilon}$, $C_{2\varepsilon}$, $C_{3\varepsilon}$, and C_μ are constants, with values of 1.44, 1.92, 1.0, and 0.09, respectively. σ_k, σ_ε are the turbulent Prontes numbers of the turbulent kinetic energy, k, and the specific dissipation rate, ε, with values of σ_k = 1.0 and σ_ε = 1.3. S_k and S_ε are user-defined source items.

2.2. Geometric Configurations and Computational Conditions

The coiled tubing is wrapped around a drum, sticking one end into the gooseneck guide. The control cabin controls the tubing, which enters the well through the injector head. A one-layer coiled-tubing-wound drum is shown in Figure 1. Due to the repeatability of the coiled tubing on a drum, a one-unit spiral section was selected as the research object, as shown in Figure 2. The inside diameter of the helical tubing is d, and its radius is r; the diameter of the drum is D, its radius is R, and the pitch is S. Since the coils are tightly wound, the pitch is equal to the inner diameter of the CT, that is, $P = d$. The curvature ratio is defined as the diameter ratio of the spiral tube to the tubing reel, that is, $\lambda = d/D = r/R$.

The diameters of the coils and tubing are the same as in the flow experiments conducted by Zhou [30–32]; nine numerical models—M1 to M9—were established, as shown in Table 1. In this study, water and gas were used as the working fluids to compare the experimental results. The rheological properties of the fluids are based on sample data at ambient temperatures. Water was selected as the liquid phase, with a density of 998.200 kg/m^3 and a viscosity of 1.003 mPa·s. Air was selected as the gas phase, with a density of 1.205 kg/m^3 and a viscosity of 0.0181 mPa·s.

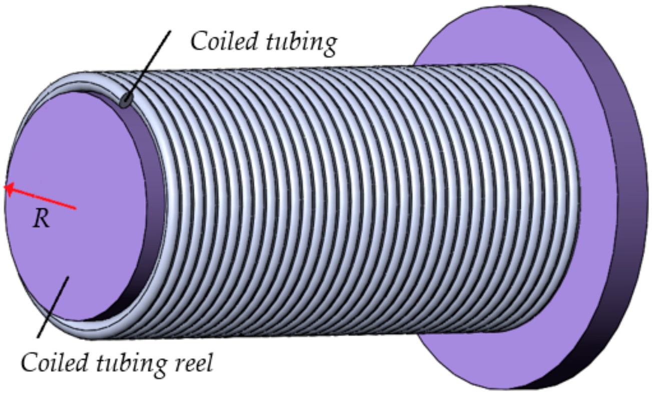

Figure 1. Schematic diagram of one-layer CT.

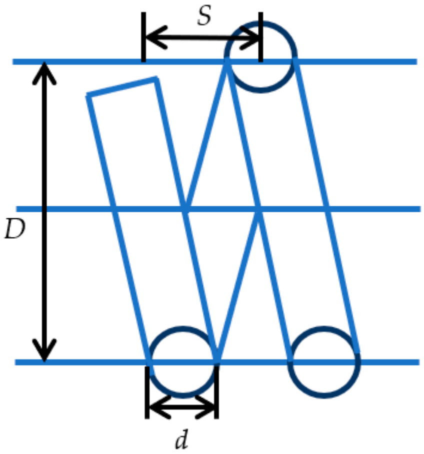

Figure 2. Geometric parameters of element helical segment.

Table 1. Geometric dimensions of coils and tubing.

Model	CT Diameter	Coil Diameters	Curvature Ratio
	d (in)	*D* (in)	d/*D*
M1	0.435	3.6	0.010
M2	0.435	1.8	0.019
M3	0.435	1.2	0.031
M4	0.435	0.5	0.076
M5	0.810	48	0.017
M6	0.810	72	0.011
M7	1.188	72	0.017
M8	2.063	111	0.019
M9	1.532	82	0.018

The meshing of the helical tube was stretched to a 3D block by a 2D auxiliary block and swept. Then, structured meshing was performed. The inlet region was divided into O-shaped meshing, as shown in Figure 3. The near-wall region was processed with a refined mesh and treated using non-equilibrium wall functions. The non-slip boundary condition was used at the tubing wall. The inlet and outlet boundaries were set as velocity- and pressure-outlet boundary conditions, respectively. The CFD simulations of a two-phase flow in CT were performed with Fluent 19.0 to study the flow behavior of gas and liquid phases [33]. The finite volume method was used to discretize the governing equations, and the phase-coupled SIMPLE scheme discretized the pressure–velocity coupling [34].

To obtain satisfactory accuracy and better convergence, all results were simulated using a constant time step of 1×10^{-5} s on an HP-T7000 workstation (1T hard disk, 8 GB RAM, and 3.6 GHz CPU).

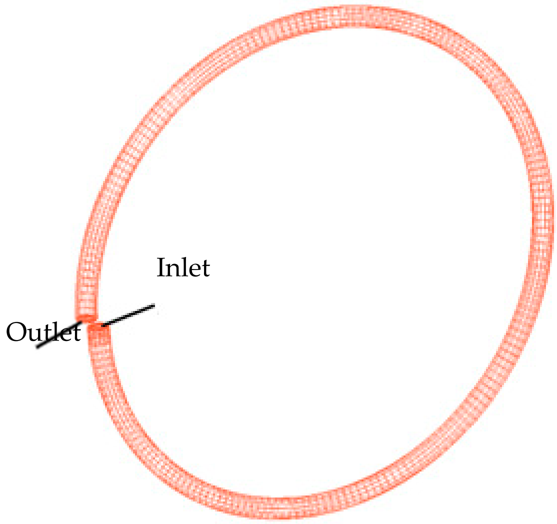

Figure 3. Computational grid of element helical tube.

3. Results and Discussion

3.1. Sensitivity of Grid Size to Simulation Results

Primary studies were carried out to investigate the variations in the simulation results, using grid number variation for the pressure drop under different gas void fractions. Taking M2 as an example, with the inlet velocity v_{in} set as 5 m/s, the pressure drop along the tubing at four grid sizes (85,000, 98,000, 113,000, and 126,000) is shown in Figure 4. When the number of grid points increases from 85,000 to 98,000, the pressure drop increases by 15.2%; when the grid size increases from 98,000 to 113,000, the pressure drop changes by 1.2%; when the grid size increases from 11,3000 to 126,000, the pressure drop changes by 0.8%. It was observed that when the number of grid points increases from 98,000 to 126,000, the pressure drop does not change significantly. By considering the calculation accuracy and computational cost, the number of grid points was finally chosen as 98,000.

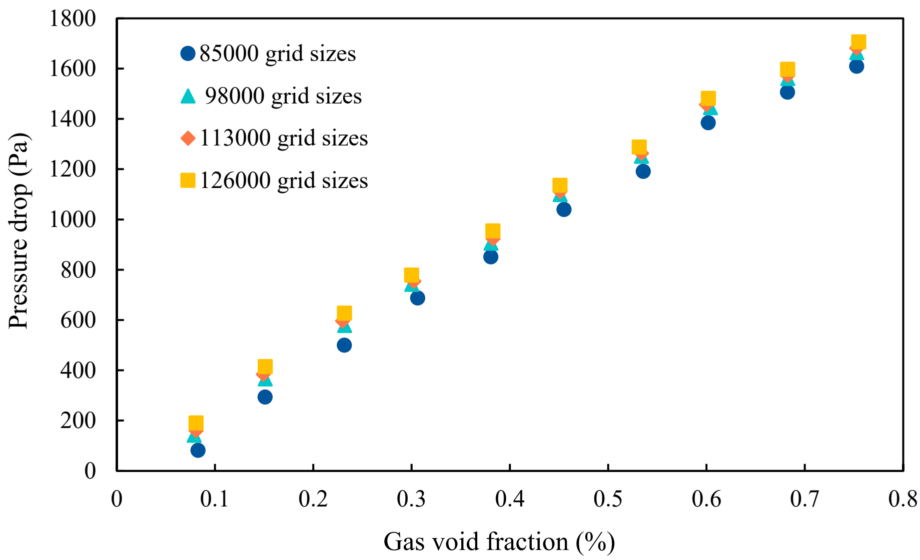

Figure 4. Simulated pressure drop along the tubing at four grid sizes.

3.2. Model Validation between Simulations and Experiments

Comparisons of the simulated and measured values of the Fanning friction factor, f, in CT for the M1–M9 tubing sizes are shown in Figure 5 as a function of the Reynolds number, Re. In Zhou's experiment, water was used as the fluidizing agent; the density was 998.20 kg/m^3, and the viscosity was 1.003 mPa·s. The Reynolds number was 5000 < Re < 230,000, and the flow was turbulent in the tubing for all sizes in the experiment.

For the Newtonian fluids, the Fanning friction factor, f, for smooth CT in a turbulent flow, can be calculated from the following equation:

$$f = \frac{0.084 \left(d/D \right)^{0.1}}{\mathrm{Re}^{0.2}} \tag{8}$$

Figure 5 shows that the simulation results exhibit good agreement with the experimental data reported in the literature. As the Reynolds number increases, the Fanning friction factor decreases. Average error (Avg. error) and standard deviation (RMS) are used to characterize the error between the simulation and experimental values to verify the validity of the numerical model. Average error (Avg. error) reflects the difference between the simulated results and experimental value and can be expressed as:

$$Avg.error = \frac{1}{\mathrm{n}} \sum\nolimits_{\mathrm{n}=1}^{\mathrm{n}} \left| \frac{\Delta P_{EXP}}{\Delta P_{SIM}} - 1 \right| \tag{9}$$

where ΔP_{EXP} is the experimental data of the pressure drop, ΔP_{SIM} is the simulated value of the pressure drop, and n is the amount of data.

The standard deviation (RMS) reflects the stability of the error between the simulated and experimental data and can be expressed as follows:

$$RMS = \sqrt{\frac{\sum_{n=1}^{n} \left(error_i - Avg.error \right)^2}{n-1}} \tag{10}$$

The average error and standard deviation between the simulation and experimental values for the M1–M9 coiled tubing are shown in Table 2. We can see from the data that the maximum average error and standard deviation are 2.14% and 0.006, respectively. The simulation results agree well with the experimental results, which proves that the established simulation model and the above numerical method can simulate the fluid flow in coiled tubing.

Table 2. Average error and standard deviation between simulation and experimental values for M1–M9 coiled tubing.

Model	Avg. Error	RMS
M1	1.11%	0.0029
M2	0.88%	0.0035
M3	1.57%	0.0053
M4	1.21%	0.0060
M5	0.72%	0.0027
M6	0.78%	0.0027
M7	2.14%	0.0052
M8	1.92%	0.0052
M9	1.43%	0.0063

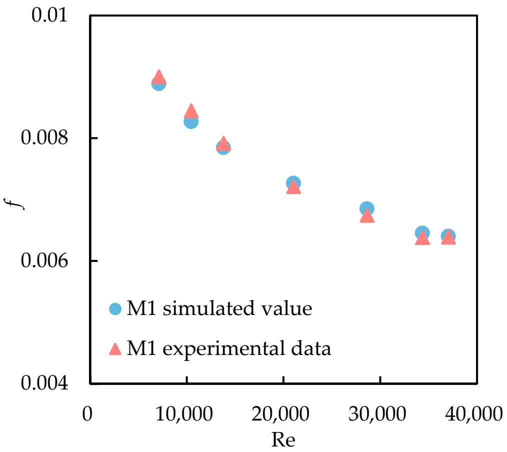

(**a**) M1 (d = 0.435 in, *D* = 3.6 in).

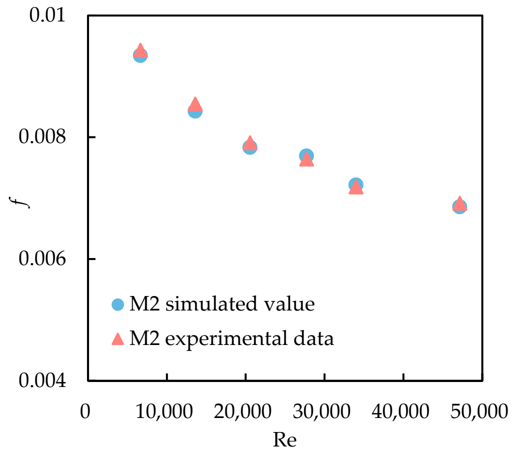

(**b**) M2 (d = 0.435 in, *D* = 1.8 in).

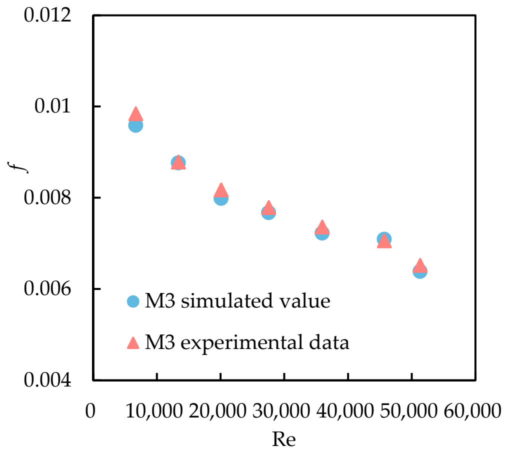

(**c**) M3 (d = 0.435 in, *D* = 1.2 in).

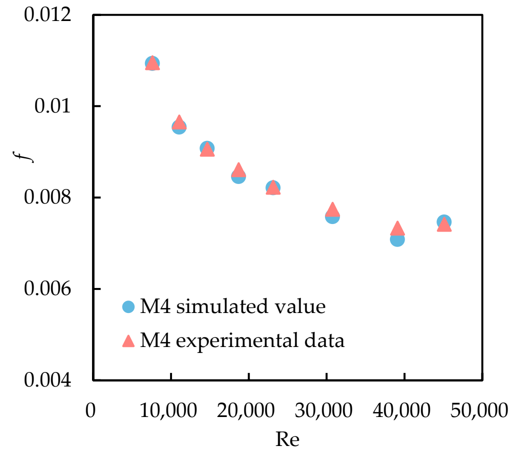

(**d**) M4 (d = 0.435 in, *D* = 0.5 in).

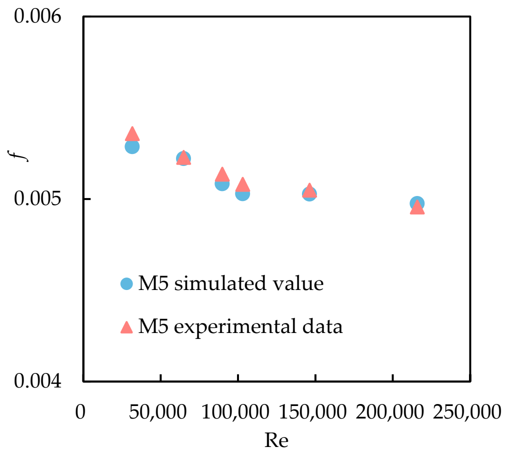

(**e**) M5 (d = 0.810 in, *D* = 48 in).

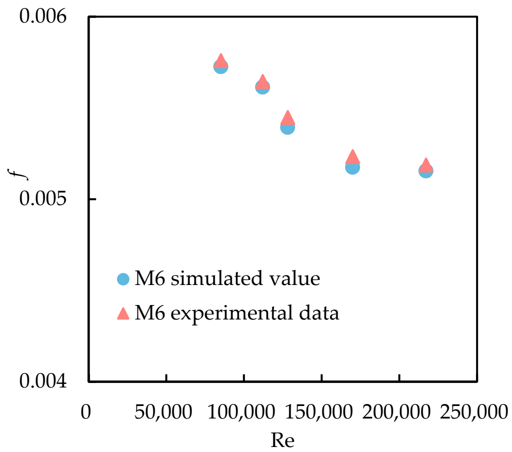

(**f**) M6 (d = 0.810 in, *D* = 72 in).

Figure 5. *Cont.*

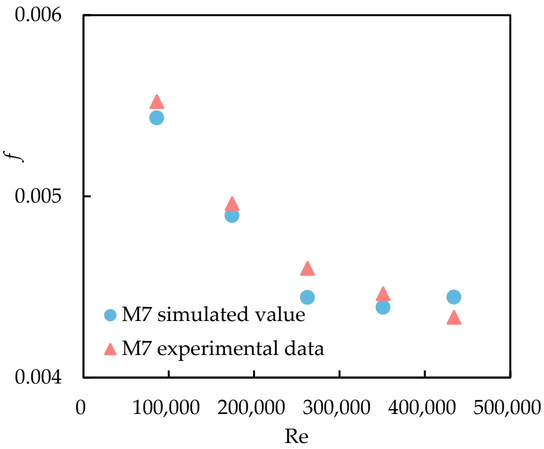

(**g**) M7 (d = 1.188 in, *D* = 72 in).

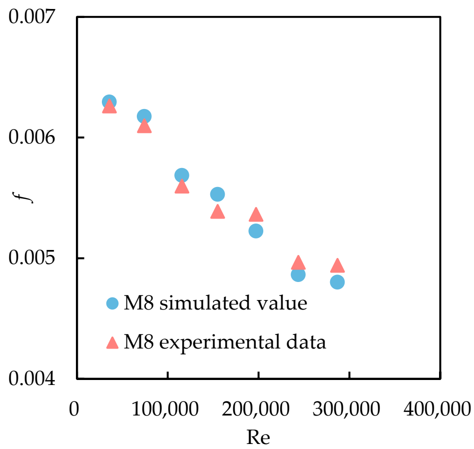

(**h**) M8 (d = 2.063 in, *D* = 111 in).

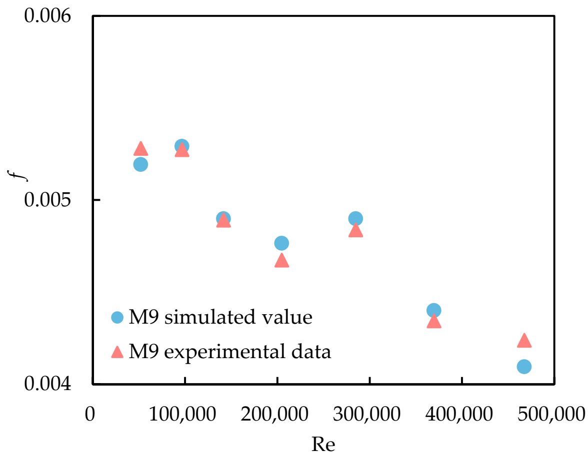

(**i**) M9 (d = 1.532 in, *D* = 82 in).

Figure 5. Comparison between the simulated and experimental friction factor for M1–M9 coiled tubing.

3.3. Axial Velocity Distribution

The inlet velocity, v_{in}, was set to 10 m/s, and the gas void fraction, α, was set to 0.3; then, the fluid velocity distribution was analyzed. The variations in the gas and liquid axial velocity are shown in Figure 6 with the circumferential position. The gas and liquid phase velocities decrease first and then rise along the axial direction. This is because the fluid first flows upward, but since the direction of gravity is opposite to the flow direction, the fluid needs to overcome gravity, which leads to a downward trend in the velocity of the gas–liquid phase fluid. When the fluid flowed at 180° of the CT, the fluid flowed downward. At this time, the gravity direction was consistent with the flow direction, and the velocity of the gas–liquid fluid began to increase continuously.

The axial velocity of gas and liquid at the outlet is lower than at the inlet. This is because the fluid flow has to overcome friction and the energy is attenuated. To describe the velocity difference in a gas–liquid two-phase fluid, the ratio of gas velocity to liquid velocity, that is, the slip velocity ratio, is introduced. The slip velocity ratio can be expressed as:

$$S = \frac{u_g}{u_l} \tag{11}$$

where u_g and u_l are the true velocities of gas and liquid, respectively.

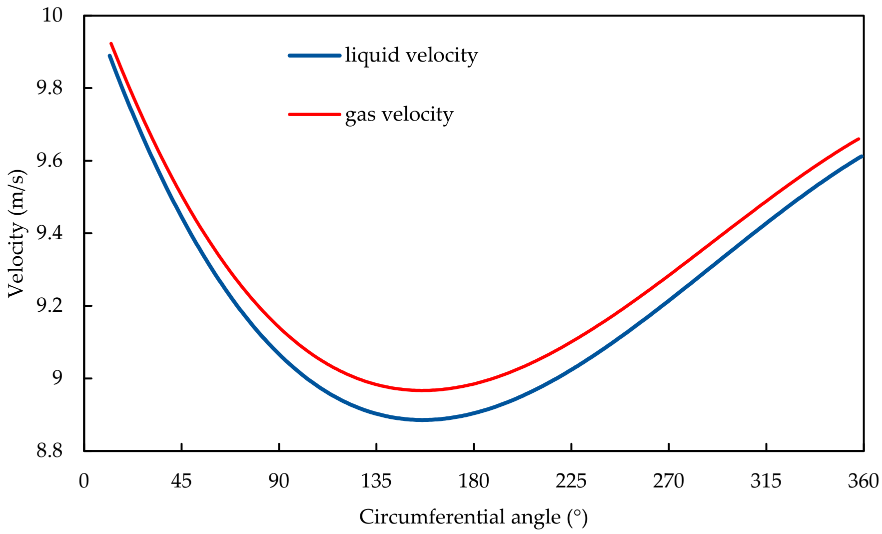

Figure 6. Gas and liquid axial velocity with the circumferential position.

Figure 7 illustrates the variations in the slip velocity ratio along the mainstream direction. The gas–liquid slip velocity ratio is always greater than 1; this is because the flow resistance of gas and liquid is different due to their different viscosities. Gas velocity is not equal to liquid velocity. The velocity difference thus changes significantly as the fluid flows, and the slip velocity ratio increases rapidly to 1.15. The virtual mass force of the gas phase to the liquid phase increases with the difference between the gas and liquid phase velocities. The increase in liquid velocity is slightly higher than that of the gas velocity; therefore, the slip velocity ratio begins to decrease slowly.

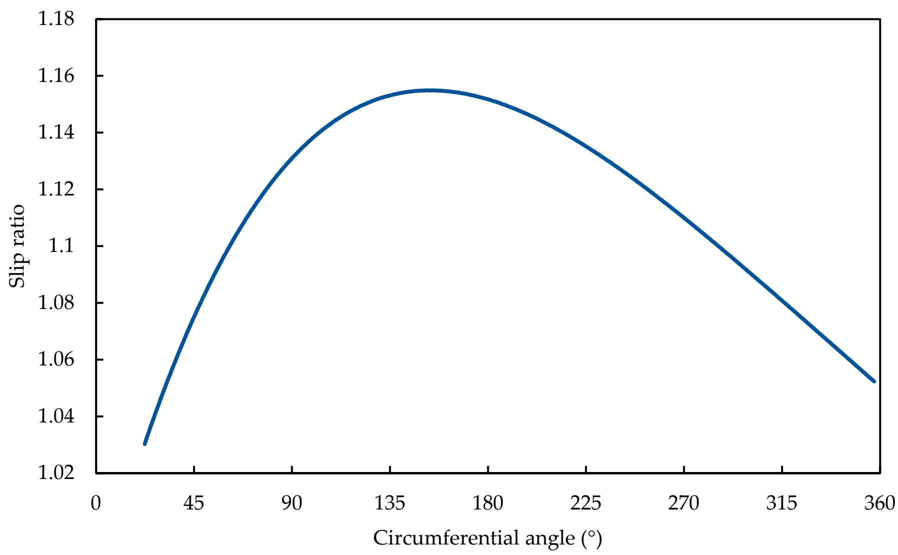

Figure 7. Slip velocity ratio with different circumferential angles.

3.4. Velocity Distribution in Cross-Section

An X–Y coordinate system was established for the spiral section to analyze the flow in the cross-sections of CT, as shown in Figure 8. The outlet and inlet were located at 0°, and the fluid flows were in a counterclockwise direction. Cross-sections A, B, C, and D are perpendicular to each other. The angle between cross-section A and the exit is 45°, and cross-sections B, C, and D have angles of 135°, 225°, and 315° from the exit, respectively. The direction of gravity is negative along the X-axis, and the magnitude is $-9.8\ \mathrm{m/s^2}$. O is the origin of the coordinate axis; the position close to origin O is the inner side (in); the position far from origin O is the outer side (ex).

The contour plots of liquid velocity at different cross-sections of spiral tubing are shown in Figure 9. The velocity has a D-shaped step distribution; the liquid velocity near the tube inside is the lowest, with the highest velocity occurring near the outside of the tube. The liquid phase velocity distribution on the upper and lower sides is nearly symmetrical. The red area in the figure means that the maximum velocity zone is off-center and is closer to the outside of the tube, which is induced by the centrifugal forces in the flow. We can see from the contour of 45° cross-section A that the velocity core area is small, and the degree of inward depression is also tiny. As the fluid flows, the velocity of the fluid in the spiral tubes is enhanced by centrifugal forces. Moreover, it can be seen that the degree of inward depression in the core area is substantial, and the mainstream core area presents a "crescent shape" at the 225° cross-section C.

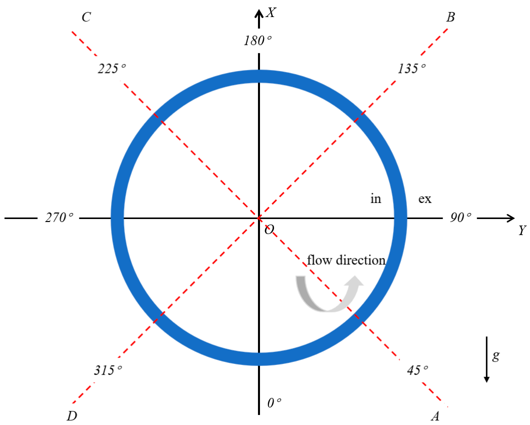

Figure 8. Profile of CT cross-sections.

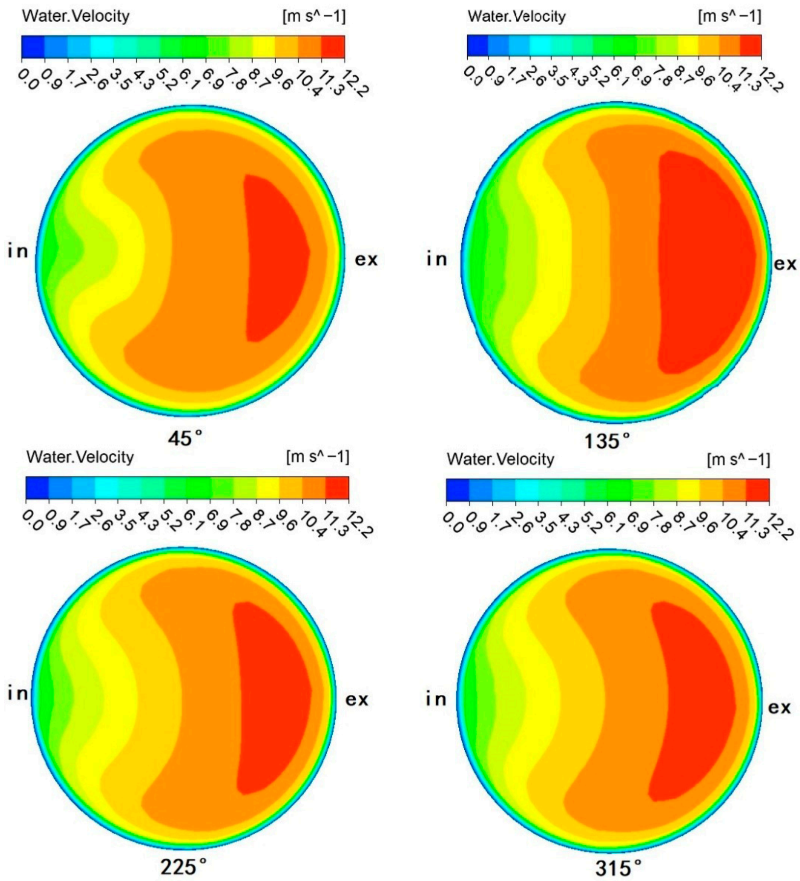

Figure 9. Simulated contours of liquid velocity at different cross-sections (v_{in} = 10 m/s, α = 0.3).

3.5. Characteristics of Secondary Flow

The variations in the radial velocity of the liquid at cross-sections A, B, C, and D are shown in Figure 10. As can be seen, the fluid not only has an axial mainstream flow but also a radial flow perpendicular to the mainstream direction. This is because the fluid in the spiral tube is subjected to a centrifugal force and the inner fluid is thrown to the outer wall. In order to maintain the continuity of the fluid, an up-and-down vortex structure is formed. Since the upper and lower vortices are in the secondary-flow field, we call this the secondary flow.

The ratio of the maximum radial velocity to axial mainstream average velocity was used to characterize the secondary-flow intensity by Ishigaki [35]. The secondary-flow intensity is defined by:

$$s = \frac{v_{r\max}}{v_{\text{axi}}} \tag{12}$$

where s is the secondary-flow intensity, v_{rmax} is the maximum radial velocity, and v_{axi} is the average velocity of the axial mainstream.

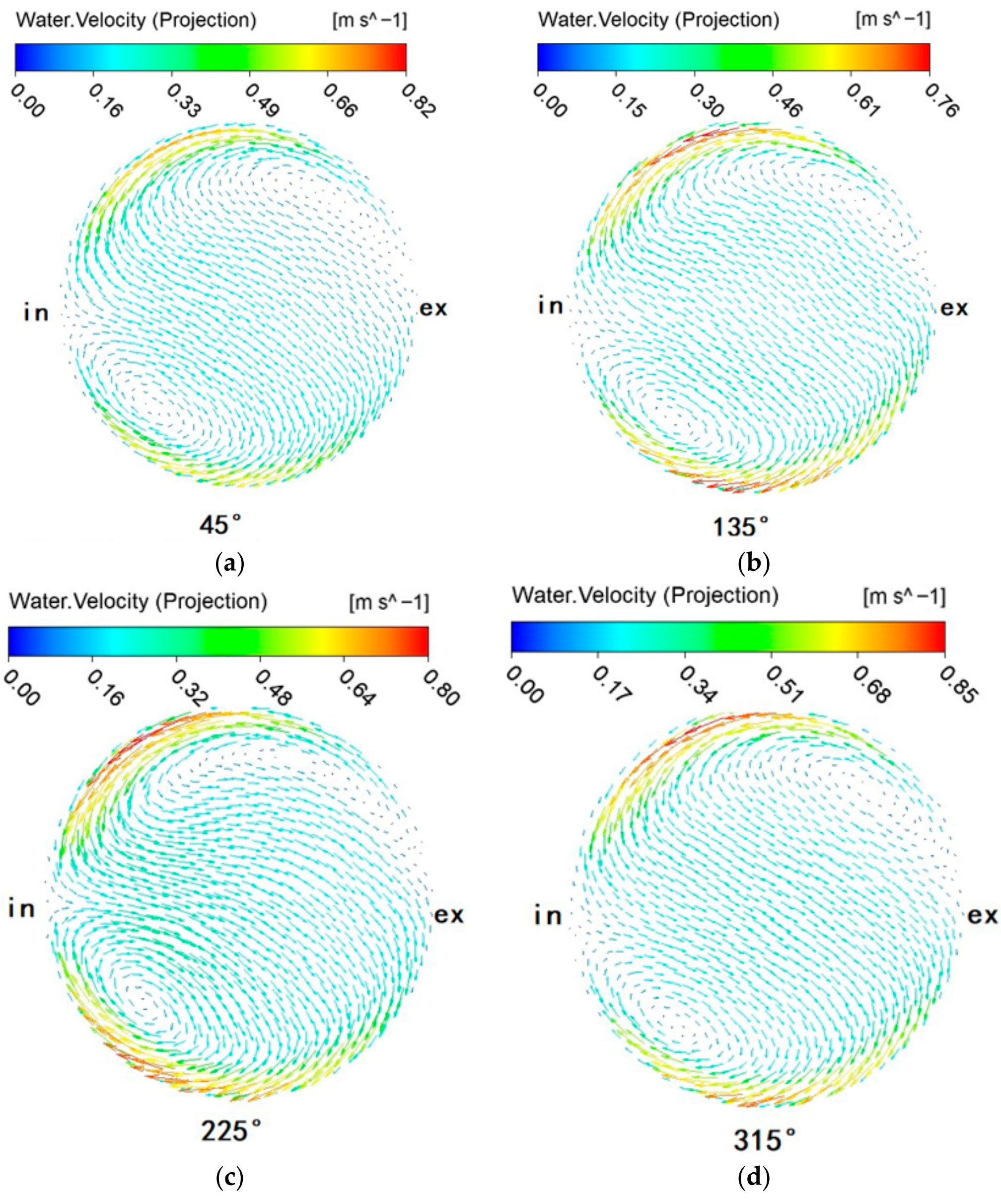

Figure 10. Radial velocity vector of liquid at cross-sections (**a**–**d**) (v_{in} = 10 m/s, α = 0.3).

At the circumferential angles of 45°, 135°, 225°, and 315°, the maximum radial velocities are 0.82 m/s, 0.76 m/s, 0.80 m/s, and 0.85 m/s, respectively; the axial velocities are 9.7 m/s, 8.7 m/s, 8.9 m/s, and 9.5 m/s. Moreover, the maximum values of the secondary-flow velocity are 0.084, 0.087, 0.089, and 0.090 of the average axial velocities at cross-sections A, B, C, and D, respectively.

Figure 11 shows the variations in the secondary-flow intensity with a circumferential angle; the intensity of the secondary flow increases along the flow direction. This is mostly because the curved structure of the spiral tube accelerates the fluid near the outer wall, increasing the maximum radial velocity.

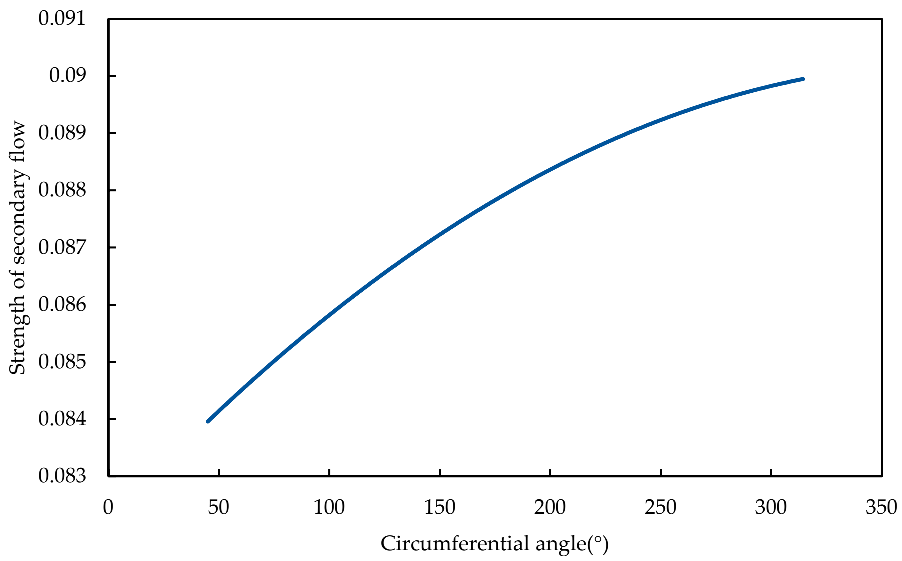

Figure 11. Secondary-flow intensity with circumferential angle.

3.6. Distribution of Gas–Liquid Phase in Cross-Sections

The distribution of the gas and liquid phases in cross-sections A, B, C, and D, with a gas void fraction of 0.3, is shown in Figure 12. It can be seen from 45° cross-section A, that the distribution of the gas–liquid phases is relatively concentrated and has prominent separation characteristics. The gas phase gathers on the inside of the pipe, and the liquid phase gathers on the outside due to gravity's action. At the same time, under the action of centrifugal force, the liquid phase moves to the outside of the tubing, and the gas phase gathers on the inside of the tubing.

As can be seen from the contour of 135° cross-section B, the gas and liquid phases have begun to mix; the liquid phase continues to flow to the outside of the tube as a function of centrifugal force, and the gas phase gradually gathers to the outside of the tube under the drive of the liquid phase. The flow is divided into upper and lower flow regions because of the presence of secondary flows.

The gas distribution at 225° cross-section C shows that the gas phase's content has decreased near the origin O, and two incomplete eddy currents have appeared. Moreover, two vortices can be seen at 315° cross-section D, and the liquid phase gathers on the outside of the tubing, while the gas phase gathers on the inside and in the region of these two vortices.

The gas holdup fluctuates up and down with the change in the circumferential position. However, the fluctuation is slight and the overall trend is stable, as shown in Figure 13. This is because the liquid is thrown to the outside of the helix tube under the influence of centrifugal force. In contrast, the gas is distributed on the inside due to its low density. The distribution of the gas content along the tubing is relatively stable and is consistent with the previous research on two-phase flow distributions in conventional-size spiral tubes.

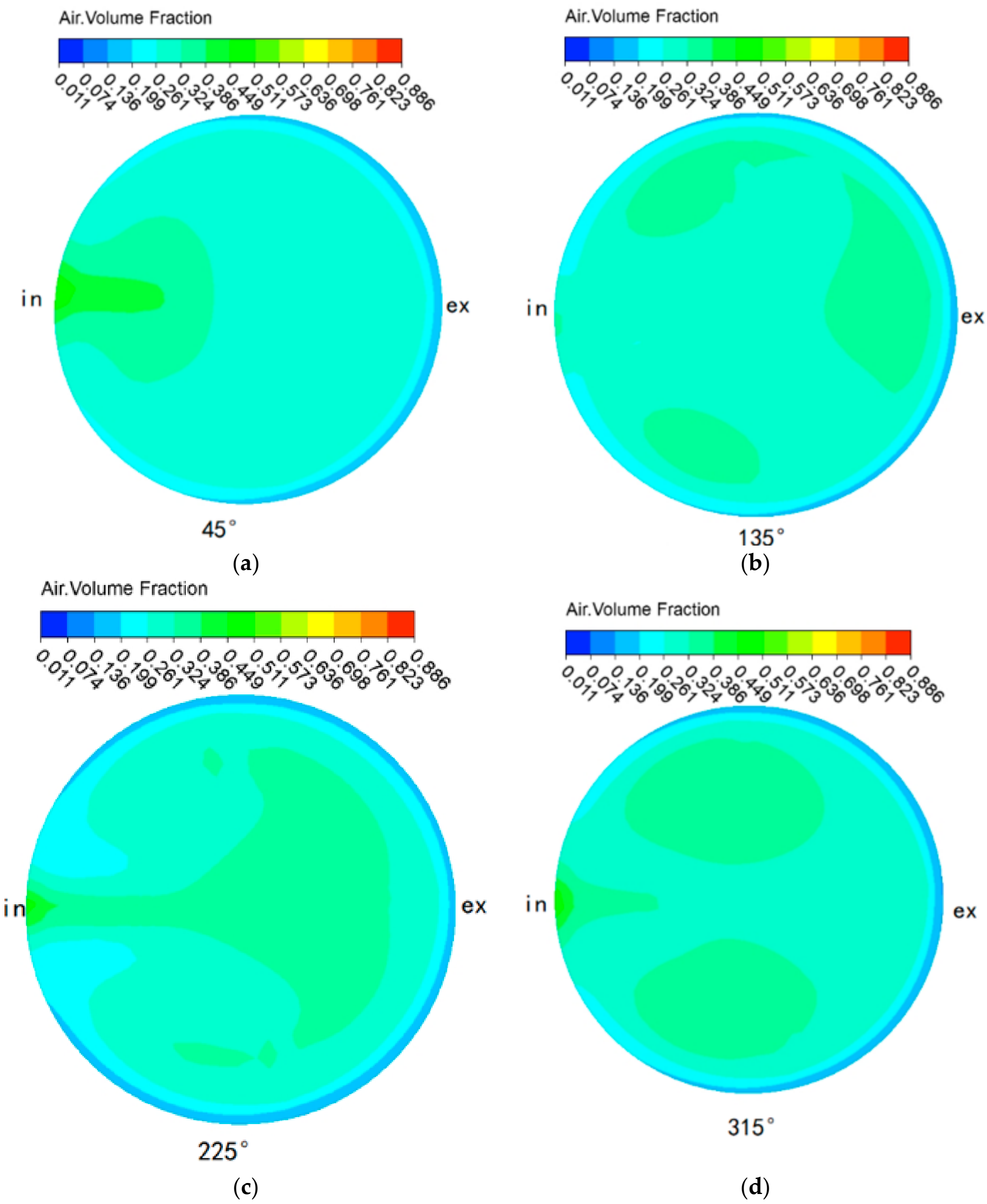

Figure 12. Distribution of gas and liquid phases in cross-sections (**a**–**d**).

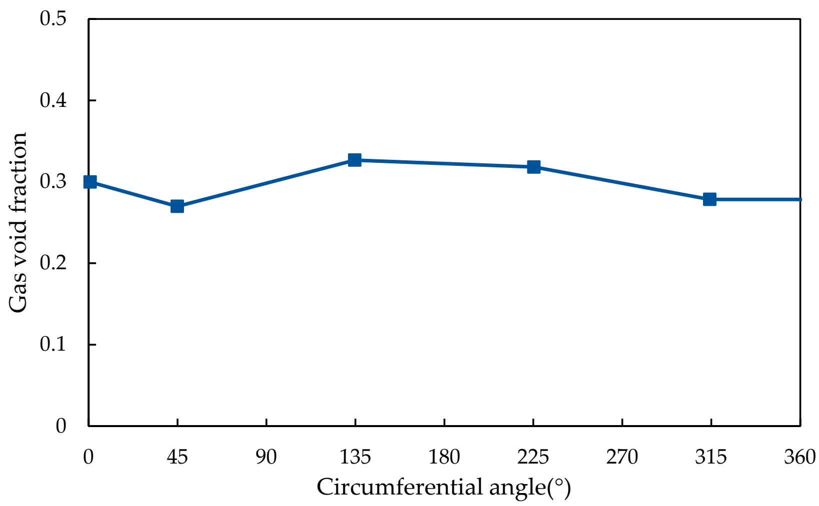

Figure 13. Gas void fraction with circumferential angle.

4. Conclusions

The flow behaviors of gas and liquid in spiral tubes were simulated using the Eulerian–Eulerian two-phase fluid model, with the standard k-ε model for the turbulent viscosity of the gas–liquid fluid. Velocity distributions and phase distributions were investigated.

The gas and liquid phase velocities decrease and rise along the axial direction. By the action of centrifugal force, the radial velocity, perpendicular to the axial velocity direction, leads to a secondary flow, and the secondary-flow intensity increases along the length of the tubing. The liquid velocity near the inside of the CT is the lowest, while it is highest near the outside of the CT; the liquid velocity distribution on the upper and lower sides is nearly symmetrical. The gas–liquid phase is separated, and the gas phase is mainly concentrated on the inside of the tube, while the liquid phase is concentrated on the outside. Under the action of a secondary flow, the gas and liquid phases form two obvious symmetric vortices. This paper is helpful in understanding the complex flow behavior of a gas–liquid two-phase flow in CT. The research results can lay a theoretical foundation for the establishment of a frictional pressure drop model of a CT system. It is worth noting, however, that the simulation in this study did not consider the influence of the rheological properties of non-Newtonian fluids. Future studies will focus on the influence of the shear stress and shear dilution of non-Newtonian fluids on the flow behavior of the gas–liquid flow.

Author Contributions: Conceptualization, J.L.; validation, W.Z. and T.Y.; writing—original draft, S.S. All authors have read and agreed to the published version of the manuscript.

Funding: This work is supported by the National Natural Science Foundation of China (Grant No. 52004064), the China Postdoctoral Science Foundation (Grant No. 2021M700755), and Natural Science Foundation of Heilongjiang Province (Grant No. LH2022E028).

Institutional Review Board Statement: Not applicable.

Informed Consent Statement: Not applicable.

Data Availability Statement: Not applicable.

Conflicts of Interest: The authors declare no conflict of interest.

References

1. Eustice, I. Experiments on Stream-Line Motion in Curved Pipes. *Proc. R. Soc. Lond. Ser. A* **1911**, *85*, 119–131. [CrossRef]
2. Eustice, I. Flow of Water in Curved Pipes. *Proc. R. Soc. Lond. Ser. A* **1910**, *84*, 107–118. [CrossRef]
3. Dean, W.R.; Hurst, J.M. Note on the Motion of Fluid in a Curved Pipe. *Mathematika* **1959**, *6*, 77–85. [CrossRef]
4. Berger, S.A.; Talbot, L.; Yao, L.S. Flow in Curved Pipes. *Annu. Rev. Fluid Mech.* **1983**, *15*, 461–512. [CrossRef]
5. Willingham, J.D.; Shah, S.N. Friction Pressures of Newtonian and Non-Newtonian Fluids in Straight and Reeled Coiled Tubing. In Proceedings of the SPE/ICoTA Coiled Tubing Roundtable, Houston, TX, USA, 5–6 April 2000. [CrossRef]
6. Zhou, Y.; Shah, S.N. New Friction Factor Correlations for Non-Newtonian Fluid Flow in Coiled Tubing. *SPE Drill. Complet.* **2006**, *21*, 68–76. [CrossRef]
7. McCann, R.C.; Isias, C.G. Frictional Pressure Loss during Turbulent Flow in Coiled Tubing. In Proceedings of the SPE Gulf Coast Section/ICoTA North American Coiled Tubing Roundtable, Conroe, TX, USA, 26–28 February 1996.
8. Boersma, B.J.; Nieuwstadt, F.T.M. Large-Eddy Simulation of Turbulent Flow in a Curved Pipe. *J. Fluids Eng.-Trans. ASME* **1996**, *118*, 248–252. [CrossRef]
9. Zhang, J.K.; Li, G.S.; Huang, Z.W.; Tian, S.C.; Shi, H.Z.; Song, X.Z. Numerical Simulation on Friction Pressure Loss in Helical Coiled Tubing. *J. China Univ. Pet.* **2012**, *36*, 115–119. [CrossRef]
10. Asafa, K.A.; Shah, S.N. Effect of Coiled Tubing Buckling on Horizontal Annular Flow. In Proceedings of the SPE/ICoTA Coiled Tubing & Well Intervention Conference and Exhibition, The Woodlands, TX, USA, 27–28 March 2012.
11. Guan, F.; Ma, W.; Tu, Y.; Zhou, C.; Feng, D.; Zhou, B. An Experimental Study of Flow Behavior of Coiled Tubing Drilling System. *Adv. Mech. Eng.* **2014**, *1*, 935159. [CrossRef]
12. Wang, F.; Li, Z.; Chen, H.; Li, S. Foam Fluid Flow Analysis in Helical Coiled Tubing Using CFD. *Procedia Eng.* **2015**, *126*, 696–700. [CrossRef]
13. Pereira, C.E.G.; da Cruz, G.A.; Pereira Filho, L.; Justino, L.R.; Paraiso, E.C.H.; Rocha, J.M.; Calçada, L.A.; Scheid, C.M. Experimental Analysis of Pressure Drop in the Flow of Newtonian Fluid in Coiled Tubing. *J. Pet. Sci. Eng.* **2019**, *179*, 565–573. [CrossRef]

14. Oliveira, B.R.; Leal, B.C.; Pereira Filho, L.; Borges, R.F.d.O.; Paraíso, E.d.C.H.; Magalhães, S.D.C.; Rocha, J.M.; Calçada, L.A.; Scheid, C.M. A Model to Calculate the Pressure Loss of Newtonian and Non-Newtonian Fluids Flow in Coiled Tubing Operations. *J. Pet. Sci. Eng.* **2021**, *204*, 10864. [CrossRef]
15. Martinelli, R.C.; Nelson, D.B. Prediction of Pressure Drop during Forced-Circulation of Boiling Water. *Trans. ASME* **1948**, *70*, 695–702.
16. Lockhart, R.W.; Martinelli, R.C. Proposed Correlation of Data for Isothermal Two-Phase Two Component Flow in Pipes. *Chem. Eng. Prog.* **1949**, *45*, 39–45.
17. Akagawa, K.; Sakaguchi, T.; Ueda, M. Study on a Gas- Liquid Two- Phase Flow in Helically Coiled Tubes. *Bull. JSME* **1971**, *14*, 564–571. [CrossRef]
18. Bi, Q.; Chen, T.; Luo, Y.; Zheng, J. Frictional Pressure Drop of Steam-Water Two-Phase Flow in Helical Coils with Small Helix Diameter of HTR-10. *Chin. J. Nucl. Sci. Eng.* **1996**, *3*, 208–213. [CrossRef]
19. Xin, R.C.; Awwad, A.; Dong, Z.F.; Ebadian, M.A. An Experimental Study of Single-Phase and Two-Phase Flow Pressure Drop in Annular Helicoidal Pipes. *Int. J. Heat Fluid Flow* **1997**, *18*, 482–488. [CrossRef]
20. Santini, L.; Cioncolini, A.; Lombardi, C.; Ricotti, M. Two-Phase Pressure Drops in a Helically Coiled Steam Generator. *Int. J. Heat Mass Transf.* **2008**, *51*, 4926–4939. [CrossRef]
21. Guo, L.; Feng, Z.; Chen, X. An Experimental Investigation of the Frictional Pressure Drop of Steam-Water Two-Phase Flow in Helical Coils. *Int. J. Heat Mass Transf.* **2001**, *44*, 2601–2610. [CrossRef]
22. Colombo, M.; Cammi, A.; Guédon, G.R.; Inzoli, F.; Ricotti, M.E. CFD Study of an Air-Water Flow inside Helically Coiled Pipes. *Prog. Nucl. Energy* **2015**, *85*, 462–472. [CrossRef]
23. Cioncolini, A.; Santini, L. Two-Phase Pressure Drop Prediction in Helically Coiled Steam Generators for Nuclear Power Applications. *Int. J. Heat Mass Transf.* **2016**, *100*, 825–834. [CrossRef]
24. Zhao, H.; Li, X.; Wu, X. New Friction Factor Equations Developed for Turbulent Flows in Rough Helical Tubes. *Int. J. Heat Mass Transf.* **2016**, *95*, 525–534. [CrossRef]
25. Xiao, Y.; Hu, Z.; Chen, S.; Gu, H. Experimental Study of Two-Phase Frictional Pressure Drop of Steam-Water in Helically Coiled Tubes with Small Coil Diameters at High Pressure. *Appl. Therm. Eng.* **2018**, *132*, 18–29. [CrossRef]
26. Wu, J.; Li, X.; Liu, H.; Zhao, K.; Liu, S. Calculation Method of Gas–Liquid Two-Phase Boiling Heat Transfer in Helically-Coiled Tube Based on Separated Phase Flow Model. *Int. J. Heat Mass Transf.* **2020**, *161*, 114381. [CrossRef]
27. Wu, J.; Li, Z.; Li, S.; Chen, Y.; Liu, S.; Xia, C.; Chen, Y. Numerical Simulation Research on Two-Phase Flow Boiling Heat Transfer in Helically Coiled Tube. *Nucl. Eng. Des.* **2022**, *395*, 111827. [CrossRef]
28. Gidaspow, D. *Multiphase Flow and Fluidization: Continuum and Kinetic Theory Descriptions*; Academic Press: New York, NY, USA, 2012.
29. Wilcox, D.C. *Turbulence Modeling for CFD*; DCW Industries: La Canada, CA, USA, 1998.
30. Zhou, Y.; Shah, S.N. Rheological Properties and Frictional Pressure Loss of Drilling, Completion, and Stimulation Fluids in Coiled Tubing. *J. Fluids Eng.-Trans. ASME* **2004**, *126*, 153–161. [CrossRef]
31. Zhou, Y. *Theoretical and Experimental Studies of Power-Law Fluid Flow in Coiled Tubing*; University of Oklahoma: Norman, Oklahoma, 2006.
32. Shah, S.; Zhou, Y.; Bailey, M.; Hernandez, J. Correlations to Predict Frictional Pressure Loss of Hydraulic-Fracturing Slurry in Coiled Tubing. *SPE Prod. Oper.* **2009**, *24*, 381–395. [CrossRef]
33. FLUENT. *ANSYS FLUENT User's Guide*; ANSYS, Inc. Release 19.0: Canonsburg, PA, USA, 2018.
34. Ogugbue, C.C.; Shah, S.N. Laminar and Turbulent Friction Factors for Annular Flow of Drag-Reducing Polymer Solutions in Coiled-Tubing Operations. *SPE Drill. Complet.* **2011**, *26*, 506–518. [CrossRef]
35. Ishigaki, H. Laminar Flow in Rotating Curved Pipes. *J. Fluid Mech.* **1996**, *329*, 373–388. [CrossRef]